NEUROSCIENCE

Epitope-preserving magnified analysis of proteome (eMAP)

Joha Park[1,2]†, Sarim Khan[1,3]†, Dae Hee Yun[1,2,4]†, Taeyun Ku[1,2]‡, Katherine L. Villa[2,4]§, Jiachen E. Lee[2,4], Qiangge Zhang[4,5,6], Juhyuk Park[1,2,7,8], Guoping Feng[4,5,6], Elly Nedivi[2,4]*, Kwanghun Chung[1,2,4,7,8,9]*

Synthetic tissue-hydrogel methods have enabled superresolution investigation of biological systems using diffraction-limited microscopy. However, chemical modification by fixatives can cause loss of antigenicity, limiting molecular interrogation of the tissue gel. Here, we present epitope-preserving magnified analysis of proteome (eMAP) that uses purely physical tissue-gel hybridization to minimize the loss of antigenicity while allowing permanent anchoring of biomolecules. We achieved success rates of 96% and 94% with synaptic antibodies for mouse and marmoset brains, respectively. Maximal preservation of antigenicity allows imaging of nanoscopic architectures in 1000-fold expanded tissues without additional signal amplification. eMAP-processed tissue gel can endure repeated staining and destaining without epitope loss or structural damage, enabling highly multiplexed proteomic analysis. We demonstrated the utility of eMAP as a nanoscopic proteomic interrogation tool by investigating molecular heterogeneity in inhibitory synapses in the mouse brain neocortex and characterizing the spatial distributions of synaptic proteins within synapses in mouse and marmoset brains.

INTRODUCTION

Over the past decade, hydrogel-tissue hybridization techniques have enabled new approaches in molecular imaging and phenotyping of biological systems (*1*–*5*). These methods synthesize acrylic polymer networks inside the tissue specimen to mechanically support tissue architecture and anchor endogenous biomolecules at their physiological location. To prevent loss of biomolecules during subsequent tissue clearing or expansion, chemical fixatives have been used to covalently link individual biomolecules to the acrylic polymer mesh. In this process, formaldehyde, the most commonly used tissue fixative, forms highly reactive methylols with amine groups in the endogenous biomolecules. We and others have used acrylamide as a major building block of polymeric networks because acrylamide can readily react with methylol to form an irreversible methylene bridge (*1*, *2*, *6*, *7*). The high concentrations (4 to 30%) of acrylamide used in these methods ensure that most of the methylol-carrying molecules are covalently anchored to the polymer mesh, effectively preventing their loss in the subsequent delipidation, physical tissue expansion, and even harsh destaining steps.

This covalent hydrogel-tissue fusion strategy has been widely adopted to enable interrogation of a broad range of biological systems, including mammalian organs, human clinical samples, plants, and invertebrates (*2*, *6*–*11*). However, all the methods based on this strategy suffer from a fundamental side effect of the covalent anchoring: chemical modification of biomolecules. Endogenous proteins have many amine-containing amino acids on their surface, which can react with formaldehyde and subsequently with acrylamide. The chemical modification of these surface moieties can cause epitope damage. In addition, long acrylic polymer chains linked to epitopes or nearby the epitope sites can physically block antibody-epitope interactions. These undesirable effects of the covalent tissue-hydrogel fusion cause the loss of a wide range of epitopes, substantially limiting the pool of commercially available antibodies that can be used to interrogate biological systems.

This drawback becomes particularly problematic when studying complex biomolecular machinery, such as chemical synapses. Each synapse (less than 0.5 μm^3 in volume) contains hundreds of unique protein species highly organized in three dimensions (3D). The compositions and the nanoscopic organization of the synaptic proteins (SyPs) determine the function of individual synapses within a specific neural circuit. Synthetic gel–based superresolution imaging techniques, such as magnified analysis of proteome (MAP) (*6*) and expansion microscopy (ExM) (*2*), provide the opportunity to interrogate the molecular diversity and heterogeneity in synapses at nanoscopic resolution with diffraction-limited microscopy. However, our limited ability to recognize specific molecules has hampered this investigation.

Here, we present epitope-preserving MAP (eMAP) technology that enables exceptional preservation of epitopes in an expandable tissue-gel hybrid. eMAP is designed to avoid the chemical conjugation of acrylamide monomers to biomolecules to minimize the loss of antigenicity. Instead of chemical crosslinking, we demonstrated that purely physical hydrogel-tissue hybridization can robustly anchor biomolecules and preserve their epitopes and nanoscopic organizations in a 4- to 10-fold linearly expandable tissue gel. eMAP-processed mouse and marmoset brain tissues were compatible with 96% (49 of 51) and 94% (46 of 49) of antibodies against SyPs tested, respectively. All the tested antibodies provided bright and highly specific signals in 1000-fold volumetrically expanded tissues without any additional signal amplification. eMAP allowed us to perform multiplexed, multiround nanoscopic characterization of individual synapses in both

[1]Institute for Medical Engineering and Science, Massachusetts Institute of Technology (MIT), Cambridge, MA 02139, USA. [2]Picower Institute for Learning and Memory, MIT, Cambridge, MA 02139, USA. [3]Department of Chemical Engineering, Indian Institute of Technology (IIT), Roorkee, Uttarakhand 247667, India. [4]Department of Brain and Cognitive Sciences, MIT, Cambridge, MA 02139, USA. [5]McGovern Institute for Brain Research, MIT, Cambridge, MA 02139, USA. [6]Broad Institute of MIT and Harvard University, Cambridge, MA 02142, USA. [7]Department of Chemical Engineering, MIT, Cambridge, MA 02142, USA. [8]Center for Nanomedicine, Institute for Basic Science (IBS), Seoul 03722, Republic of Korea. [9]Graduate Program of Nano Biomedical Engineering (NanoBME), Advanced Science Institute, Yonsei University, Seoul 03722, Republic of Korea.
*Corresponding author. Email: nedivi@mit.edu (E.N.); khchung@mit.edu (K.C.)
†These authors contributed equally to this work.
‡Present address: KAIST Graduate School of Medical Science and Engineering, Daejeon 34141, Republic of Korea.
§Present address: Tevard Biosciences, Cambridge, MA 02139, USA.

4× and 10× linearly expanded tissues using a diffraction-limited microscope and commercial antibodies. We demonstrated the utility of eMAP for quantitative studies of the heterogeneity in molecular composition of inhibitory synapses and the nanoscopic organization of various SyPs within a single synapse in mouse and marmoset brains.

RESULTS

Physical hybridization minimizes loss of antigenicity

We hypothesized that the loss of antigenicity in covalently fused synthetic tissue gel is caused by the chemical bonding of acrylic monomers to amino acid residues within or nearby the epitope site (Fig. 1A). The direct chemical tethering of acrylic monomers to the epitope site can substantially alter the weak interactions (e.g., electrostatic and Van der Waals interactions) crucial in the antigen-antibody binding process, causing loss of antigenicity. The chemically bonded acrylic monomers within or nearby the epitope site can also recruit bulky proteins or polymer chains, resulting in physical masking of the epitope, which hinders antibody-antigen binding (Fig. 1A).

To minimize the loss of antigenicity in the tissue-gel hybridization process, we modified the original MAP protocol to remove formaldehyde during the gelation step. Instead of transcardial perfusion of

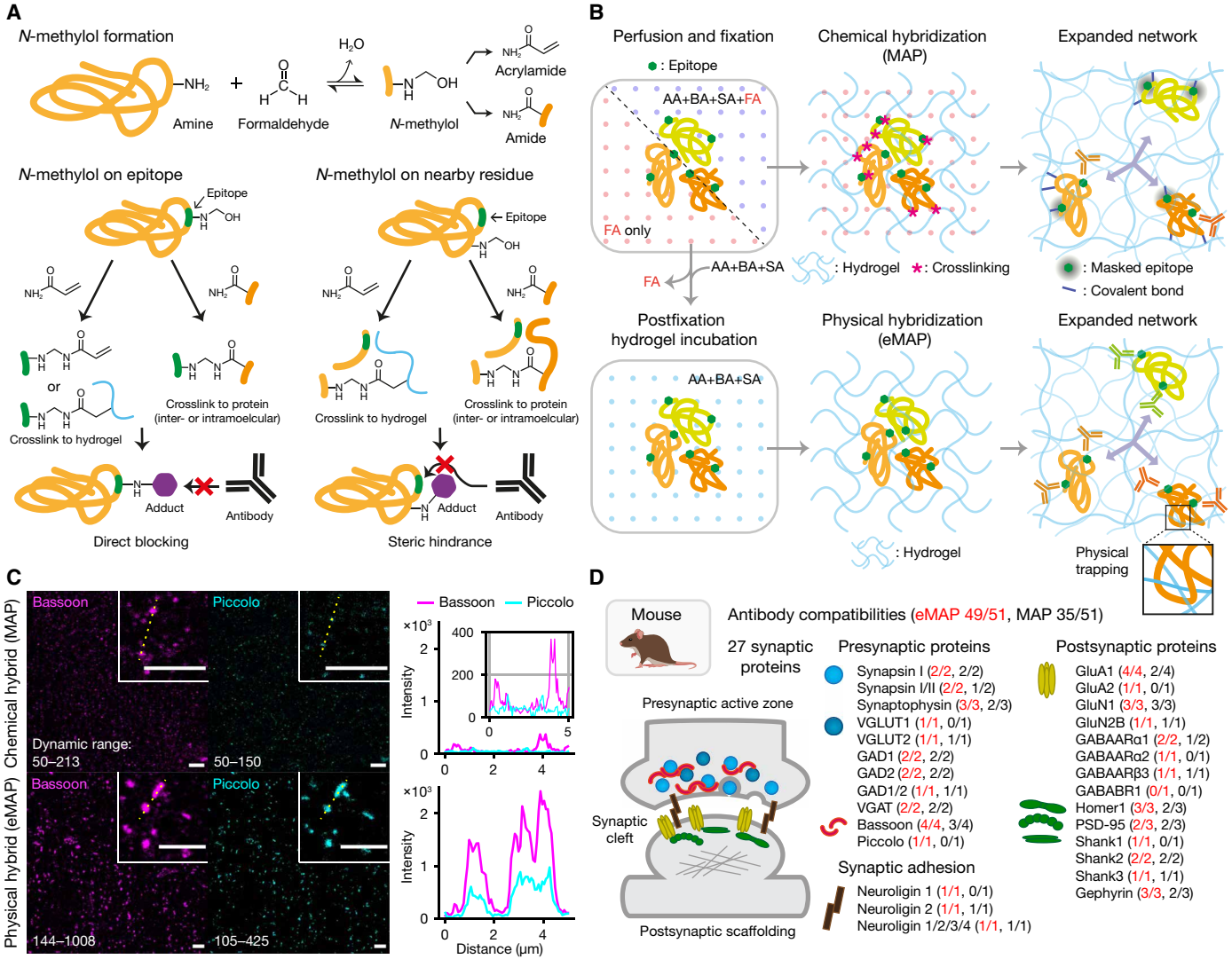

Fig. 1. eMAP maximally preserves antigenicity by minimizing chemical alteration of epitopes. (**A**) Schematics illustrating the modes of epitope damage in tissue-gel hybridization. The primary amines on proteins react with formaldehyde to form methylol, which can subsequently react with acrylamide or primary amide groups of polypeptides to form irreversible methylene bridges. These chemical modifications lead to direct or indirect damage of epitopes, causing the loss of antigenicity. (**B**) Schematics showing the original MAP and eMAP procedures. In the original MAP, biomolecules are chemically crosslinked to the swellable gel. On the other hand, biomolecules are physically trapped in the swellable gel in eMAP. AA, acrylamide; BA, bis-acrylamide; SA, sodium acrylate; FA, formaldehyde. (**C**) Comparison of immunohistochemistry signal profiles between the chemical (MAP) and physical (eMAP) hybrids. Bassoon (magenta) and Piccolo (cyan) antibodies were coimmunolabeled, and the images were taken using identical imaging settings. The images are displayed in different dynamic ranges, and the ranges are shown in the lower left corners. The inset images show 4× digitally zoomed subregions identical in the two channels and contain the yellow dotted line for drawing intensity profiles shown on the right. The inset line plot for the chemical hybrid shows the same line intensity profile but with a reduced *y*-axis scale. Scale bars, 5 μm. (**D**) Antibody compatibilities in the chemical (MAP) and physical (eMAP) hybrids. Fifty-one antibodies targeting the 27 SyPs were evaluated.

the hydrogel monomer solution containing 4% formaldehyde, eMAP starts with a formaldehyde-fixed tissue. The sample is thoroughly washed to remove any excess formaldehyde before gelation. During this extensive washing step, the unreacted methylols can release formaldehyde because the methylol formation reaction is reversible, restoring the native property of the respective amino acids. Next, we incubate the tissue in a hydrogel monomer solution containing 30% acrylamide, 10% sodium acrylate, 0.1% bis-acrylamide, and 0.03% VA-044. In the absence of formaldehyde in the hydrogel monomer solution, acrylic monomers cannot react with endogenous biomolecules; hence, the biomolecules are not covalently anchored to the swellable gel network. This unique gelation enables the polymeric chains to form physical entanglements with biomolecules (Fig. 1B) (*12*). The tissue-gel hybrid synthesized in the absence of formaldehyde is subsequently incubated in a buffer solution containing SDS at 95°C for 10 min to dissociate protein complexes. The heat-treated tissue gel is then expanded in deionized (DI) water. We use the term "physical hybridization" to describe the process of synthesizing a physically crosslinked swellable gel in a fixed tissue sample.

We compared the antigenicity of chemical and physical hybrids by staining and imaging them using the same imaging settings. Notably, we prepared both hybrids using tissues that originated from the same animal to control the base antigenicity. Because transcardial perfusion of the MAP monomer solution is incompatible with the physical hybrid preparation, we made slight modifications to the protocol to recapitulate the chemical alteration of epitopes occurring in the original MAP protocol. In short, a mouse brain perfused with 4% formaldehyde was immediately hemisected and then incubated in a buffer containing both the eMAP hydrogel monomers and 4% formaldehyde for chemical hybrid preparation. The opposite hemisphere was reserved for physical hybrid preparation. To test the antigenicity, we stained the chemical and physical hybrids with Bassoon and Piccolo antibodies that are not compatible with the original MAP protocol. Bassoon and Piccolo are both components of the presynaptic cytoskeletal matrix and are expected to localize closely (*13*). As expected, the chemical hybrid exhibited mostly nonspecific signals that are weak and not concordant between the two target channels, indicating that the antibodies do not work with the chemical hybrid (Fig. 1C, top). In contrast, bright synaptic puncta were clearly visible in the two channels and they showed high concordance (Fig. 1C, bottom). In addition, we asked whether signal quality could further improve the physical hybrid for antibodies that show poor or moderate signal quality in MAP-processed tissues. In all three Homer1 antibodies we tested in this experiment, the signal-to-noise ratio was greatly improved and the signals were noticeably brighter in the physical hybrid at the same laser power (fig. S1, A and B, and table S1). Together, we confirmed that the chemical alteration of tissue gel in the presence of both acrylamide and formaldehyde can lead to loss of antigenicity, while the physical hybridization in eMAP can enhance antibody labeling in tissue gel by minimizing the loss.

One of the notable drawbacks of the synthetic gel–based techniques has been a limited compatibility with antibodies targeting SyPs. As a rigorous test, we selected 51 antibodies targeting 27 different SyPs that either are commonly cited for studying the synaptome or were readily available to us at the time of the experiments (table S1). For cross-validation, we grouped two or three antibodies produced from different host species into an experimental set for costaining if they (i) share a target or (ii) have closely related targets (e.g., paralogs) expected to be localized in the vicinity. We tested 33 sets of antibodies and used three biological replicates of mouse brains for testing each set. The success or failure of the antibody labeling was determined by three independent experts based on the colocalization of signals and overall staining patterns and then confirmed for consistency. The chemically hybridized mouse tissues (MAP) were compatible with only 35 of 51 antibodies, covering 21 SyP targets (Fig. 1D and table S1). The targets failed included key proteins (e.g., Piccolo, Shank1, and GluA2) that have been implicated in neurological disorders (*14*–*16*). In contrast, physically hybridized tissues (eMAP) were compatible with 49 of 51 SyP antibodies tested, covering a wider array of 26 SyP targets including those key proteins (Fig. 1D, fig. S1C, and table S1). In addition, we systematically compared the signal quality of antibody labeling in the chemical and physical hybrids in a quantitative manner. We calculated Pearson's correlation coefficient of the colabeling images of the paired antibodies (fig. S1D). In general, the correlation coefficient was greater in the physical hybrid, and the increase was more prominent for the antibodies that are compatible only with eMAP. For the antibodies that work with both hybridization methods, we also compared the maximum intensity value (99.99 percentile to exclude outlier pixels) of the images taken at the same imaging settings. The maximum signal intensity range was greater by up to ~8.3-fold in the physical hybrid for most antibodies we tested (fig. S1E), indicating that eMAP-processed tissues exhibit much brighter signals because of maximally preserved epitopes.

eMAP reveals feature-rich details of nanoscopic molecular composition without signal amplification

We found that eMAP can provide exceptionally high quality images even in 1000-fold volumetrically expanded tissues without any additional signal amplification. Using recursive hydrogel embedding, we achieved ~10× linear expansion (9.72 ± 0.11, $n = 3$) of the eMAP-processed tissue gel with four rounds of embedding (Fig. 2A). To validate the effective resolution achieved by ~10× linear expansion, we eMAP-processed a mouse brain tissue with four rounds of embedding and performed immunostaining for β-tubulin to visualize microtubules to measure the transverse peak-to-peak distance of the microtubule sidewall. For the eMAP-processed mouse brain tissue, the distance between the sidewall peaks was 48.5 ± 16.9 nm (fig. S2), which is in line with the results from iterative ExM (*8*). This suggests that we can successfully achieve superresolution imaging by homogeneous recursive physical expansion of the tissue specimen.

The repetitive embedding renders the tissues mechanically robust because of the high density of interwoven polymer chains in the hybrid despite approximately 1000-fold volumetric expansion. The robustness of eMAP-processed tissue gel allows easy handling and post-expansion antibody labeling with great compatibility. We confirmed that antibodies can easily diffuse in and out of the tissue-gel hybrid, indicating that the pores within the entangled high-density meshes are large enough for the transport of free macromolecules. Unexpectedly, simple primary and secondary antibody staining of the 1000-fold expanded tissues with the tested antibodies provided high-quality images without any additional signal amplification. This unique feature of eMAP eliminates the need for sophisticated fluorescence signal amplification or custom probe development, allowing easy adoption of the technology by any biology laboratory.

The high expansion factor and exceptional antibody compatibility of eMAP allowed us to investigate the spatial organization of different

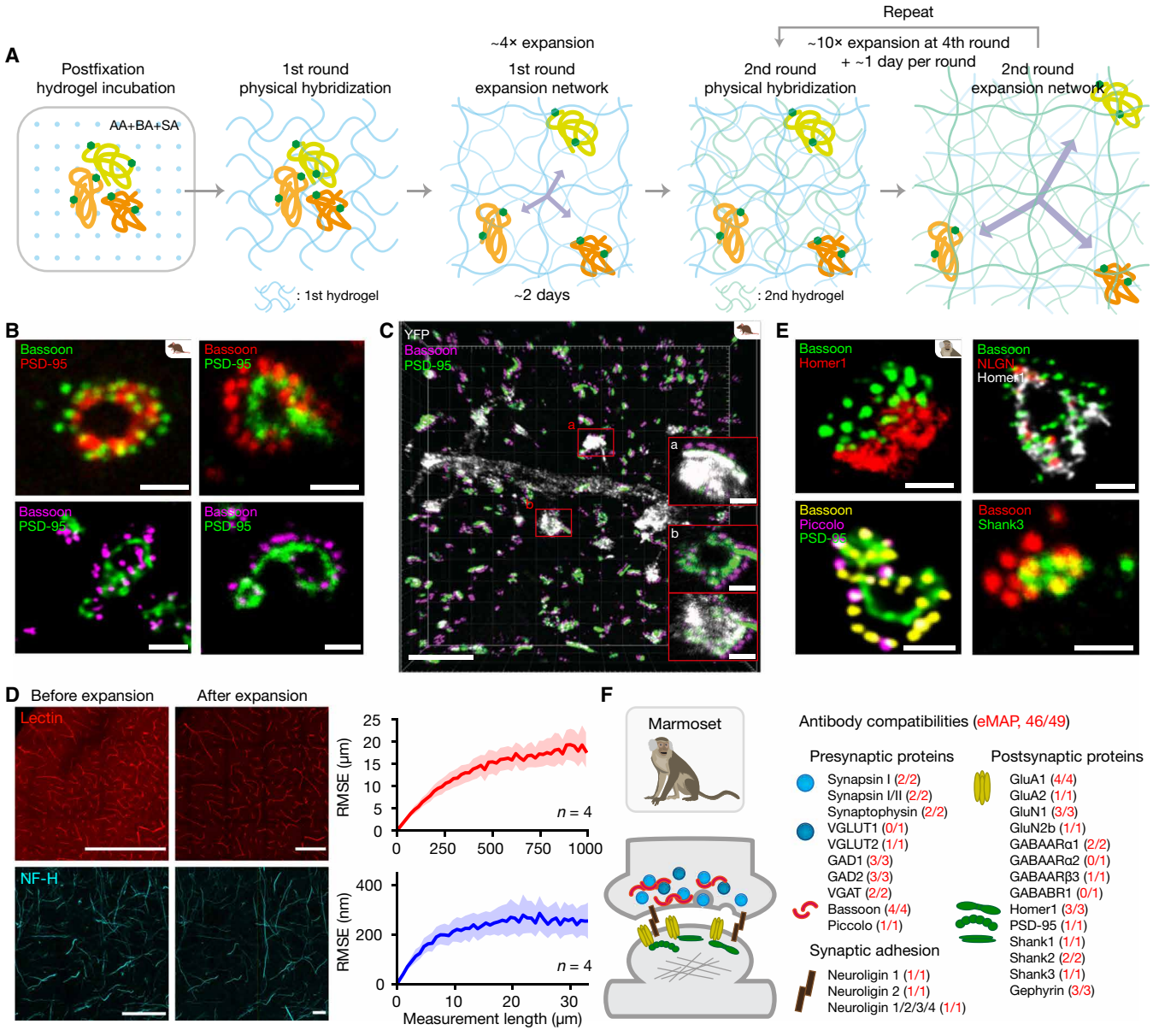

Fig. 2. eMAP offers high expansion factors by recursive embedding while preserving the spatial organization of molecules. (**A**) Schematic of the recursive embedding of an eMAP-processed tissue. (**B**) Individual synapses in eMAP-processed, 10× linearly expanded mouse brain tissues visualized by different sets of Bassoon and PSD-95 antibodies: Bassoon SYSY 141004 and PSD-95 NeuroMab 75-028 (top), and Bassoon SYSY 141003 and PSD-95 NeuroMab 75-028 (bottom). Scale bars, 200 nm (2 μm in expanded). (**C**) 3D-rendered image of a 50-μm-thick (5 μm before expansion) mouse brain slice stained with anti-YFP (white), Bassoon (magenta), and PSD-95 (green) antibodies. Scale bars, 500 nm (5 μm in expanded). (A) and (B) are inset images of respective dendritic spines highlighted in the 3D-rendered image. Scale bars, 200 nm (2 μm in expanded). (**D**) Images showing Lectin-stained (top) and NF-H–stained (bottom) tissues before and after expansion. Scale bars, 500 μm (Lectin) and 50 μm (NF-H). The plots on the right show the root mean square error (RMSE) at different measurement lengths mesoscale (top) and microscale (bottom). (**E**) Individual synapses in eMAP-processed, 10× linearly expanded marmoset brain tissues visualized by different sets of antibodies. Scale bars, 200 nm (2 μm in expanded). (**F**) Antibody compatibility in eMAP-processed marmoset brain tissue for the 27 SyPs in Fig. 1D.

types of SyPs with the large library of commercial antibodies (table S1). We immunolabeled eMAP-processed mouse brain tissues for putative excitatory synapses by colabeling Bassoon and PSD-95, which are localized in the pre- and postsynaptic compartments, respectively, with different sets of antibodies (Fig. 2B). Notably, the symmetrical distribution of the discrete 3D Bassoon nanoclusters could be visualized on top of perforated PSD-95 in the synapses organized along the optical axis of the confocal microscope. Similar perforated PSD-95 distributions were visualized using stimulated emission depletion (STED) microscopy in living mice (*17*) and using serial electron microscopy in a rhesus monkey (*18*). The highly organized distribution of Bassoon nanoclusters on top of the postsynaptic compartment (PSD-95) indicates the highly isotropic nature of the nanoscale expansion in the tissue specimen. To visualize the

3D distribution of SyPs around a reference synaptic bouton, we processed a *Thy1-eYFP* (enhanced yellow fluorescent protein) mouse brain tissue (Fig. 2C). We immunolabeled for YFP, Bassoon, and PSD-95 in the tissue and found that the discrete nanoclusters of Bassoon (magenta) could be visualized on top of the green fluorescent protein (GFP)–tagged dendritic spines/boutons (white) (Fig. 2C, a), while PSD-95 (green) could be seen overlapping with the GFP-tagged synaptic boutons (Fig. 2C, b).

To validate whether eMAP retains multiscale molecular architecture without severe distortion, we imaged mouse brain slices labeled with Lectin or NF-H before and after eMAP expansion. The distortion analysis with Lectin showed that the root mean square error (RMSE) was mostly under ~4.0% across measurement lengths up to 1 mm (Fig. 2D, top). Similarly, the same analysis with NF-H showed mostly less than ~2.3% error in the range up to 30 μm (Fig. 2D, bottom). Together, these results indicate that eMAP preserves both meso- and microscale spatial organization of the proteins within the tissue.

Next, we used the eMAP protocol to visualize the ultrastructure of synapses in marmoset brain tissues using the commercially available antibodies (table S1). We achieved ~10× expansion for the marmoset brain tissue and obtained high-quality images of nanoscale synaptic structure, visualized by various SyPs across the presynaptic active zone (Bassoon and Piccolo), synaptic cleft (neurolignin), and postsynaptic scaffolding (PSD-95, Homer1, and Shank3) without signal amplification (Fig. 2E). Similar to eMAP-processed mouse brain tissues, the marmoset brain tissue was compatible with 46 of the 49 commercially available antibodies targeting SyPs, covering 24 different targets (Fig. 2F). The success of antibody labeling was determined on the basis of the staining patterns seen in the mouse brains. Thus, we demonstrated that eMAP provides a platform to study the interrelationships of a wide range of SyPs across species at nanoscopic resolution.

eMAP enables multiplexed nanoscopic interrogation of biomolecular machinery

Several lines of indirect evidence have suggested that there is heterogeneity in the molecular composition of inhibitory synapses, particularly in relation to the γ-aminobutyric acid type A ($GABA_A$) receptor (*17*, *19*, *20*). $GABA_A$ receptors are markedly complex and heterogeneous, with different subunit compositions conferring distinct pharmacological sensitivities and playing discrete roles in circuit-level plasticity (*21*, *22*). Thus, elucidating the heterogeneity in synaptic $GABA_A$ subunits could have notable therapeutic value. Unfortunately, current multiplexed SyP mapping strategies require specialized equipment or custom DNA barcoding of antibodies. In addition, the limited pool of antibodies compatible with these methods has restricted their multiplexing capabilities, hindering proteomic analysis of inhibitory synapses.

eMAP can serve as a simple yet powerful platform for multiplexed interrogation of nanoscopic molecular compositions by enabling multiround staining of the same tissue with a large library of commercially available antibodies. eMAP-processed tissues can withstand multiple rounds of labeling, mounting, imaging, and destaining without structural damage because they are mechanically robust due to the high concentration of the synthetic gel content. By registering images from the multiround immunostaining of the same tissue, eMAP can reveal a more comprehensive view of the subcellular ultrastructure. Individual sparsely labeled neurons within the volume helped with the local image registration between rounds of staining, allowing the proteomic investigation of synapses across many different areas within a large tissue volume.

To examine the issue of molecular heterogeneity in $GABA_A$ receptor content at inhibitory synapses using eMAP, we sparsely labeled individual L2/3 pyramidal neurons in the primary visual cortex by in utero electroporation at E15.5 with an eYFP cell fill, as previously published (*23*–*25*). Labeled pups were reared to ~P30 and implanted with a cranial window. After recovery, we imaged dendrites of an entire L2/3 pyramidal neuron in the binocular visual cortex by two-photon microscopy. We then fixed and eMAP-processed the tissues (~4× expansion; single embedding). The expanded tissue blocks then underwent several rounds of antibody staining and destaining, with each round containing antibody against GFP (which recognizes eYFP), to identify the imaged cell and allow registration between rounds. In addition to eYFP, round one was probed for $GABA_A$Rα1 and $GABA_A$Rβ3; round two was probed for vesicular GABA transporter (VGAT) and glutamine decarboxylase 2 (GAD2); and round three was probed for Gephyrin (Fig. 3A). After each round, the slice was imaged using a confocal microscope with a 1.3–numerical aperture (NA) objective to resolve pre- and postsynaptic puncta, and the three rounds of imaging were aligned with respect to the eYFP-filled dendrites. We scored all Gephyrin puncta within the volumes proximal to aligned dendrites for apposition with both GAD2 and VGAT to validate real inhibitory synapse presence (Fig. 3A). These synapses were then assessed for the presence of $GABA_A$ receptor subunits α1 and β3. We found that while most had both α1 and β3 subunits (56.74%), 25.15% of synapses had neither, and smaller fractions (15.09 and 3.02%, respectively) had only α1 or β3. These findings confirm that inhibitory synapses are not homogeneous in their molecular content and show that eMAP is a powerful tool for quantitative interrogation of synaptic proteome.

Next, we took advantage of eMAP's multiplexing capability to characterize the spatial distribution of protein nanoclusters within the same synapse in 10-fold linearly expanded hybrids. We eMAP-processed a mouse brain cortex tissue with four rounds of embedding and performed multirounds of immunostaining with pre- and post-SyP antibodies. In the first round, the sample was immunolabeled for Bassoon, Piccolo, and PSD-95 to visualize the distribution of active zone proteins (Bassoon and Piccolo) over the postsynaptic compartment (PSD-95) of a putative excitatory synapse (Fig. 3B, right top). In the second round of staining, we immunolabeled the tissue for PSD-95, Shank1, Shank3, and Homer1 to visualize additional postsynaptic scaffolding proteins of excitatory neurons (Fig. 3B, right bottom). PSD-95 was included in both rounds to be used as a co-registration marker to create a precise composite image of the six different proteins within the same synapse (Fig. 3C). We found that the signal intensity was uniform across the immunolabeling rounds and confirmed the complete destaining of the sample between rounds by imaging the destained tissue. Using eMAP, we were able to reveal a clear and detailed synaptic ultrastructure by visualizing six different SyPs within the single synapse. In addition, we demonstrated that eMAP can be applied for multiplexed mapping of the nanoscopic SyP distribution in marmoset brain tissues; we imaged six different SyPs through three rounds of staining of the same tissue (Fig. 3D). Together, these results demonstrate that eMAP enables multiplexed nanoscopic characterization of the proteome within a spatially compact and highly organized structure in both 4× and 10× linearly expanded tissues using commercially available antibodies and a conventional confocal microscope.

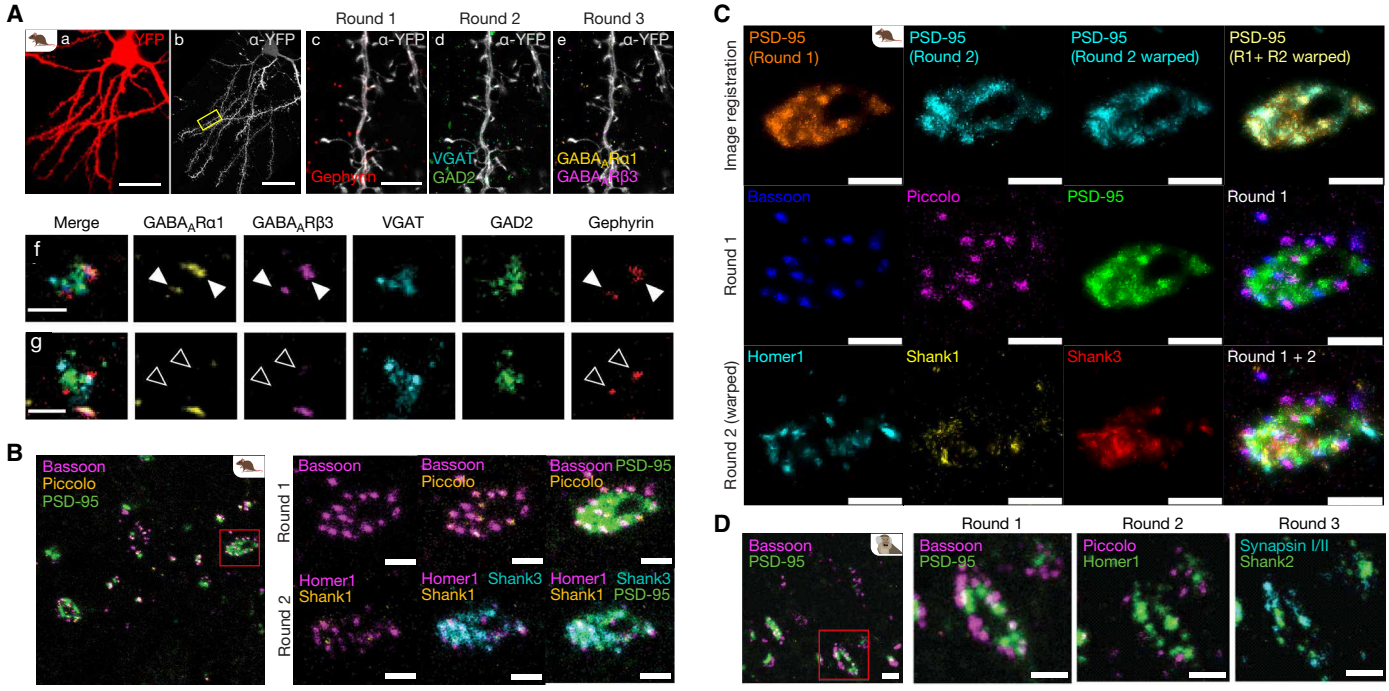

Fig. 3. eMAP enables multiplexed and integrated molecular mapping of chemical synapses at nanoscopic resolution. (**A**) (a) Two-photon imaged cell with a YFP cell fill (red) before and (b) after 4× linear expansion stained with anti-YFP (white). (c to e) Magnified view of the boxed area in (b) during multiround labeling, (c) anti-Gephyrin (red), (d) anti-VGAT (cyan), GAD2 (green), (e) anti-GABA$_A$Rα1 (yellow), and anti-GABA$_A$Rβ3 (magenta). (f) Single bouton innervating two postsynaptic Gephyrin clusters (white arrows), which contain both GABA$_A$Rα1 and β3 subunits. (g) Single bouton innervating two postsynaptic Gephyrin clusters lacking both GABA$_A$Rα1 and β3 (open arrows). Scale bars, 20 μm (a), 80 μm (b), 16 μm (c to e), and 3 μm (f and g). (**B**) Multiround staining images of an eMAP-processed mouse brain tissue. Round 1: Bassoon (magenta), Piccolo (orange), and PSD-95 (green). Round 2: Homer1 (magenta), Shank1 (orange), Shank3 (cyan), and PSD-95 (green). Magnified view of the synapse in the boxed area is shown to the right. (**C**) Separate and composite images of the same synapse in (B). Images taken from each round were co-registered to create composite images of six different proteins on the same synapse. PSD-95 channels from both rounds were used as the common channel for image registration. (**D**) Three-round staining images of an eMAP-processed marmoset brain tissue. Round 1: Bassoon (magenta) and PSD-95 (green). Round 2: Piccolo (magenta) and Homer1 (green). Round 3: Synapsin I/II (cyan) and Shank2 (green). Scale bars, 200 nm (2 μm in expanded) (B to D).

eMAP facilitates high-throughput ultrastructural analysis

Although superresolution imaging setups and freeze-fracture electron microscopy have been successfully used for studying the spatial distribution of SyPs across the brain, their widespread use has been hampered by the prohibitive costs of the equipment and complexity of the sample preparation protocols (*26*, *27*). Post-expansion antibody staining combined with the maximal preservation of epitopes in eMAP could address this challenge by enabling low cost and high-throughput imaging of the synaptic architectures using conventional confocal microscopes and the simple immunostaining procedure. Expanded eMAP-processed tissue hybrids create space around epitopes, allowing probes to bind to previously inaccessible epitope sites in tightly packed pre- and postsynaptic compartments, which provides high-quality images without signal amplification in 10× expanded tissues (*28*). Using standard confocal microscopy and eMAP, we were able to acquire a large number of superresolution images of synapses with varying viewing angles spanning side to en face views (Fig. 4A) in several different regions across the marmoset brain (fig. S3). We captured high-quality 3D images of ~50 synapses in a single *x*-*y* field of view of size 58.63 μm by 58.63 μm and a *z*-step size of 0.66 μm, with an approximate acquisition time of 300 s, thus enabling the high-content and high-throughput analysis of the synaptome.

For in-depth quantitative analysis, we chose the primary visual cortex (V1) region of the eMAP-processed marmoset brain tissue and measured the distance between pre- and post-SyPs along the synaptic axis from multiple dozens of side-view synapses. We included Bassoon and PSD-95 in all datasets to use their distance as a reference in comparing the measurements between different datasets. The distance between Bassoon and PSD-95 in the marmoset V1 was ~70.4 nm (Fig. 4B), which agrees with the distance of the mouse SyP counterparts measured by single-molecule superresolution imaging (*26*, *29*). We also report that Piccolo is located close to Bassoon at a mean relative distance of ~14 nm, which can be expected from their structural similarity and cooperative roles in the assembly and maintenance of the presynaptic active zone (Fig. 4B) (*30*). In comparison, components of excitatory neurotransmitter receptor proteins on the surface of the postsynaptic compartment, GluA1 and GluN1, are very close to the postsynaptic scaffolding protein PSD-95 (Fig. 4B).

We also measured the span of the SyPs along the axis perpendicular to the synaptic axis to examine their lateral configuration with respect to the postsynaptic scaffold. The relative span indicates whether a SyP is centrally distributed or spread over the interface of a bouton. As a proxy for the exact span, we measured the length of the major axis of an ellipse overlaid onto the segmented puncta for each channel and compared the lengths to get the relative spans with respect to PSD-95. We checked the parallelism between the major axes to ensure that we are comparing the correctly aligned lengths,

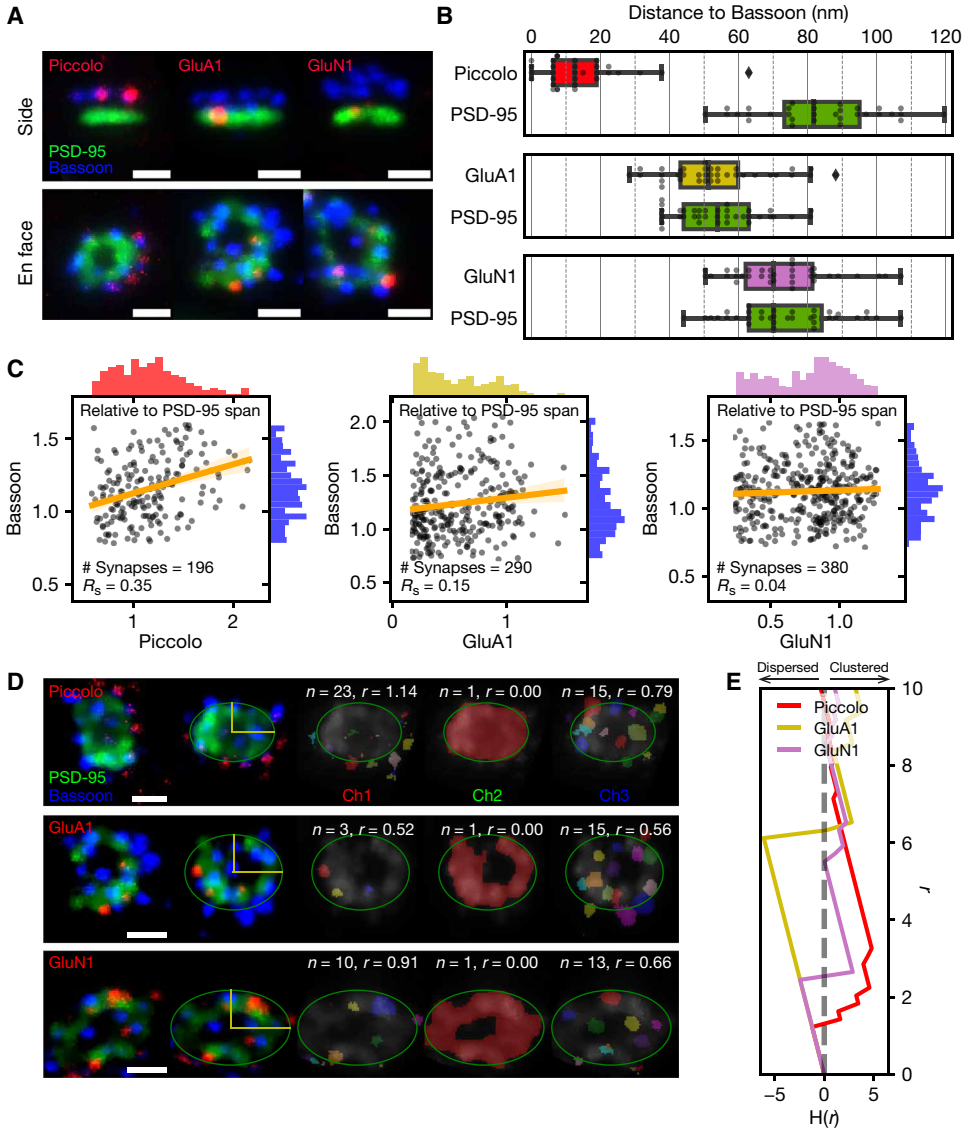

Fig. 4. eMAP facilitates high-throughput quantitative analysis of the synapses' ultrastructure. Bassoon and PSD-95 were immunolabeled in all three datasets that each contained Piccolo, GluA1, and GluN1 for a comparison between different datasets. (**A**) Example images of side and en face view synapses. Bassoon (blue), PSD-95 (green), Piccolo, GluA1, and GluN1 (red). (**B**) Estimated actual distances along the synaptic axis to Bassoon. (**C**) Relative length along the axis perpendicular to the synaptic axis with respect to the PSD-95 span. Number of synapses and the Spearman's correlation coefficient (R_s) are shown in the scatter plots. Regression lines and 95% confidence intervals are drawn in orange. Histograms for each protein are jointly depicted upon the top and right spines. (**D**) Segmentation of protein nanoclusters for each channel with en face view synapses. (Column 1) Original images. (Column 2) *X-Y* plane–rotated images with an ellipse and its major and minor axes. (Columns 3 to 5) Segmented protein nanoclusters for each channel. *n* denotes the number of segmented blobs, and *r* indicates the position of the blob centroid relative to the ellipse perimeter (see Materials and Methods). The median of *r* is shown as a representative number. (**E**) Ripley's H statistics [H(*r*)] calculated at varying radius (*r*) in pixels for the segmented blobs in (D) for each dataset. The more negative or positive statistics indicate the more dispersed or clustered spatial distribution of the blob centroids, respectively. Scale bars, 200 nm (2 μm in expanded) (A and D).

and for most synapses, the major axes were nearly parallel to each other (fig. S4). In this analysis, we observed that the major population of GluA1 nanoclusters is centrally located, while GluN1 nanoclusters show a broader distribution in terms of the relative span (Fig. 4C), consistent with previous reports (*26*, *31*). We also found that Piccolo shows a moderate positive correlation (Spearman's correlation coefficient, R_s = 0.35) with Bassoon, suggesting that their lateral distribution at synapses is co-regulated to some extent. In contrast, postsynaptic receptor subunit proteins GluA1 (R_s = 0.15) and GluN1 (R_s = 0.04) did not show notable positive correlations with Bassoon (Fig. 4C).

To further investigate the 3D architecture of the SyP nanoclusters within an individual synapse, we segmented each nanocluster in en face view synapses and assessed their radial configurations based on the centroid coordinates. We set an ellipse onto the postsynaptic scaffolding protein PSD-95 and rotated the image to align the major axis to the *x* axis. We defined the *r* value, which can tell whether a detected blob of proteins is located inside ($r < 1$), on the

perimeter ($r = 1$), or outside ($r > 1$) of the ellipse. For this particular set of synapses, we observed that Piccolo and GluN1 were located near the perimeter (Fig. 4D, top and bottom), while GluA1 was centrally distributed (Fig. 4D, middle). The Bassoon puncta were spread all over the elliptic plate of PSD-95 in all three synapses (Fig. 4D). In addition, we examined whether other SyPs (Piccolo, GluN1, and GluA1) are clustered together with Bassoon in their radial configuration by calculating the descriptive statistics of Ripley's H (*32*). We confirmed that Piccolo has a more clustered spatial distribution with Bassoon when viewed from the top (Fig. 4E), which is in line with a previous report that showed a close spatial relationship between those SyPs in the presynaptic macromolecular structure of rat neuromuscular junctions using dual-color STED microscopy (*13*). Together, we demonstrated that eMAP preserves the fine-scale molecular architecture of synapses and can facilitate high-throughput analysis of macromolecular assemblies with its exceptional compatibility with the large library of off-the-shelf antibodies and the use of a conventional imaging modality.

DISCUSSION

Here, we show that purely physical hydrogel-tissue hybridization can permanently secure biomolecules and their nanoscopic organizations in highly expandable tissue gel, enabling maximal preservation of native epitopes for superresolution proteomic imaging. We extensively tested antibodies targeting SyPs in mouse and marmoset brains and demonstrated that eMAP-processed tissues show marked antibody compatibility (49 of 51 for mouse and 46 of 49 for marmoset) and provide a robust staining signal that reveals feature-rich details of the synaptic ultrastructure. As our method efficiently exploits available epitopes by minimizing the chemical damage and physical masking, conventional antibody staining provides strong signals even in a 1000-fold volumetrically expanded specimen without the use of sophisticated signal amplification techniques. In addition, eMAP retains the beneficial features of the original MAP technique, including multiplexed post-expansion staining and multiround labeling. We envision that eMAP would also be compatible with other tissue types as the steps other than tissue-gel hybridization are mostly identical with MAP. However, rigorous validation would be required for different tissue types.

We engineered the eMAP tissue-gel hybrid to be permeable enough for antibodies to uniformly bind to their epitopes in a thick specimen while permanently anchoring endogenous proteins and forming rigid tissue gel. The proteins in the formaldehyde-fixed tissues form closed networks among themselves using methylene bridges. When linear polyacrylamide (pAAm) chains are synthesized inside the fixed tissue during the eMAP gelling process, they can penetrate the closed protein networks before they form crosslinks with other linear pAAm chains. Once the pAAm chains are fully grown and crosslinked with each other, the pAAm gel network forms physically entangled meshes with the endogenous protein network, permanently but flexibly anchoring the endogenous proteins (*5*). eMAP-processed tissues can withstand several rounds of multiplexed antibody staining and destaining cycles, enabling more comprehensive molecular phenotyping using off-the-shelf antibodies without any custom modification. SyPs closely packed within presynaptic compartments (e.g., Bassoon and Piccolo) can be easily differentiated and resolved in the eMAP-processed tissues because of its high antibody receptivity. Using eMAP, we quantitatively examined the heterogeneity of the $GABA_A$ receptor content at inhibitory synapses and also mapped the spatial distribution of multiple SyPs at the single synapse level.

In recent years, marmosets have emerged as an excellent model for studying brain function and dysfunction due to their short reproductive cycle, high cognition, and close genetic relationship to humans. Researchers have developed highly efficient genome-editing techniques to produce marmoset models of neurodevelopmental disorders (*33*–*40*). Understanding the pathophysiological impact of these mutations on the nanoscopic organization of SyPs is critical as abnormal synaptic structures are commonly found in many neurological disorders (*41*, *42*). However, the limited pool of antibodies available for primate SyPs and difficulties in interrogating nanoscopic architectures have restricted this investigation. Using eMAP, we could successfully use the commercial antibodies to acquire high-quality nanoscopic images of the targeted SyPs in the marmoset brain and quantitatively characterize their spatial organizations. However, we have only tested the antibodies with brain tissues harvested from a single marmoset due to the scarcity of marmoset brain samples. Additional studies are required to fully establish the difference in the antibody compatibility between the chemically and physically hybridized marmoset brain tissues.

We envision that the high-throughput acquisition of these rich datasets will enable holistic investigation of complex molecular machinery at nanoscopic resolution across different brain regions, genders, and ages. Recently, Cizeron *et al.* (*43*) characterized changes in SyP composition at excitatory synapses across the life span of mice. They defined several classes of synapses based on the expression pattern of PSD-95 and SAP102 and showed that the numbers and spatial distributions of these classes significantly change with age (*43*, *44*). Applying the large pool of compatible antibodies and the multiplexed imaging capability of eMAP to these studies would facilitate further characterization of these synapse subtypes and may reveal how the molecular configurations of SyPs are linked to functional differentiation of synapses.

Collectively, eMAP opens an avenue to comprehensively characterize the nanoscopic molecular structures across different tissue regions and species with greater ease. We are hopeful that the ease of sample preparation, the high compatibility with commercially available antibodies, and the use of standard imaging modalities will put our method well within reach of numerous neuroscience and biology laboratories and accelerate the study of nanoscopic molecular machinery in greater detail.

MATERIALS AND METHODS

Perfusion of the marmoset and mice brain tissues

Marmoset (12-year-old female) and Thy1-YFP-H mice (6 to 8 weeks old, male and female) were sheltered in a reversed 12-hour light/dark cycle. All the experiments were carried out with the prior approval of the Massachusetts Institute of Technology (MIT) Institutional Animal Care and Use Committee and the Division of Comparative Medicine and were in proper accordance with guidelines from the U.S. National Institutes of Health (NIH). The animals were first transcardially perfused with 4% formaldehyde in phosphate-buffered saline (PBS) at 4°C. The intact brain tissue samples were then carefully harvested from the animal carcasses. The samples were then incubated in 4% formaldehyde in PBS at 4°C for 2 to 3 days. Then, the tissue samples were left on a room temperature (RT) shaker for 1 day in PBS with 0.02% sodium azide.

Slicing and gelation

The intact brain samples were sliced into uniform 200-μm-thick slices using a vibratome (VT1000S, Leica Biosystems, Germany). The slices were then incubated in the eMAP hydrogel monomer solution [30% acrylamide (A9099, MilliporeSigma, St. Louis, MO, USA), 10% sodium acrylate (408220, MilliporeSigma), 0.1% bis-acrylamide (161-0142, Bio-Rad Laboratories, Hercules, CA, USA), and 0.03% VA-044 (w/v) (Wako Chemicals, Richmond, VA, USA) in PBS] at 4°C for 8 to 12 hours. Then, the samples were carefully placed between two glass slides using Blu-Tack adhesive (Bostik, Essendon Fields, Victoria, Australia). The empty space was filled up with additional hydrogel monomer solution. The glass slide setup was then placed inside a 50-ml Falcon tube, which was subsequently placed inside Easy-Gel (LifeCanvas Technologies, Cambridge) with nitrogen gas at 37°C for 2 to 3 hours. The tube was firmly capped and placed on a 15° incline at 36° to 37°C for 2.5 hours. To account for the exothermic nature of the gelation step, slightly lower temperature is recommended for thicker samples: ~35°C for 2-mm-thick samples and ~33°C for 3-mm-thick samples. After gelation, the cartridge was disassembled and excess gel was trimmed from around the lateral edges of the sample using a razor blade. The resulting tissue-gel hybrid sample was put in PBS at 37°C overnight for hydration.

Denaturation and recursive embeddings

The slices were incubated in a denaturation solution [6% SDS (w/v), 50 mM sodium sulfite, and 0.02% sodium azide (w/v) in PBS] at 37°C with constant shaking for 6 to 8 hours. The samples were then transferred to the preheated denaturation solution at 95°C for 10 m. Subsequently, the samples were washed in a washing solution [PBS containing 0.1% (w/v) Triton X-100 (PBST) and 0.02% (w/v) sodium azide] for 6 to 8 hours. At this point, the tissue expands linearly by ~2× (~4× in water). For the subsequent cycles of embedding, the samples were again incubated in the eMAP hydrogel monomer solution at 4°C for 12 to 24 hours. The samples were then gelled as described above but at slightly lower temperatures (35° to 36°C) to take into account more heat that would be generated during the gelation of thickened tissue gel. In between the embeddings, the samples were washed in PBST for 6 to 8 hours. The tissues were recursively incubated and gelled for three additional cycles after the initial gelation. The processed samples were incubated in DI water with shaking at RT for 2 hours with a change in solution after 1 hour. The samples expand by ~10× in the linear dimension after the expansion in DI water.

Immunostaining of brain tissues

The general protocol for immunohistochemistry of eMAP-processed brain tissues is described here. Any deviations from this protocol are detailed in appropriate sections. For typical staining, mouse brain tissue sections of 100- to 500-μm thickness were incubated with primary antibodies (typical dilution ranging from 1:100 to 1:300) in PBST at 37°C for 8 to 16 hours while shaking, followed by washing in PBST at 37°C for 3 to 5 hours with three solution exchanges. Tissues were then incubated with secondary antibodies (typical dilution ranging from 1:100 to 1:300) in PBST at 37°C for 8 to 16 hours while shaking. Samples were then washed in PBST at 37°C for 3 to 5 hours with three solution exchanges.

Following the recursive embeddings, the samples were manually sliced into 200- to 400-μm-thick vertical strips using razor blades to expose the tissue-hydrogel hybrid surface for improved antibody transport, as a thin layer of excessive pure acrylamide gel around the tissue can hamper antibody penetration. The vertical strips were then immunostained as described above, and the surface with exposed tissue-hydrogel hybrid was used for imaging.

Multiround staining

The previously stained tissues were incubated in a denaturation solution for 1 hour at 70° to 80°C to remove bound antibodies. The tissue specimen was then washed in PBST for three cycles of 2 hours each at 37°C. The samples were imaged on the microscope to confirm the complete loss in the signal from the antibodies. The tissue samples were then immunostained with a new set of antibodies.

Mounting, image acquisition, and deconvolution

The expanded specimen was placed between a petri dish and a glass-bottom Willco dish (HBSB-5030; WillCo Wells, Amsterdam, The Netherlands) using glass coverslips as spacers. To prevent the samples from drying up during image acquisition, the void space around the samples was filled up with DI water. The sample was allowed to stabilize for 30 min in the setup. Subsequently, the samples were imaged using a Leica TCS SP8 microscope system using a 63× 1.2-NA water immersion objective. The procured images were analyzed and visualized using Leica LAS X, Fiji, Imaris, and our custom scripts. The image acquisition settings were computed and implemented automatically by the lightning deconvolution package before starting the image acquisition.

Expansion factor measurement

To measure the expansion factors for each round of expansion, we imaged the tissue hybrids before and after expansion by overlaying them over a transparent grid. The transparent grid was used to ensure that each image was at the same scale before manually drawing the outlines of the tissue hybrids. These outlines were used to determine the area of the specimen using a custom script to calculate the expansion factor after each round of embedding.

Antibody validation

Three biological replicates of mouse brains were prepared for the antibody validation, with an approval by MIT Committee on Animal Care and following the NIH guidelines for the use and care of vertebrate animals. The antibodies were grouped into experimental sets based on the target and the host species. For cross-validation, we assigned two or three antibodies into an experimental set for costaining if they label the same target or closely related targets (e.g., paralogs), which are expected to be localized in proximity. In the assessment of antibody labeling, we considered the following criteria: the (i) degree of overlapping puncta, (ii) level of apparent nonspecific signals (e.g., nonspecific binding to vasculature), (iii) reproducibility in the three biological replicates, (iv) signal intensity compared to background, and (v) consistency with known staining patterns from existing publications. Three experts independently assessed the colabeling results and made a decision for the success or failure primarily based on the colocalization of signals.

To control for the source of animal tissue when comparing the chemical and physical hybrids, mouse brains perfused with 4% formaldehyde in PBS were hemisected for separate processing. Mice were first anesthetized with 0.05 ml of FatalPlus (pentobarbital) via intraperitoneal injection. Mice were then transcardially perfused with 40 ml of ice-cold PBS followed by 20 ml of ice-cold 4% formaldehyde solution in PBS. Extracted brains were incubated in a 4% formaldehyde

PBS solution on ice for 1 hour before being hemisected. Each hemisphere was then slabbed to 1-mm-thick coronal slabs using a brain matrix and razor blades. For chemical hybrid preparation, 1-mm-thick coronal slabs were incubated in the eMAP hydrogel monomer solution with additional 4% formaldehyde for 2 days at 4°C while shaking before proceeding with gelation. For physical hybrid preparation, the 1-mm-thick coronal slabs were incubated in a 4% formaldehyde PBS solution for 2 days at 4°C, which were then washed in PBS for 1 day with three solution exchanges at RT. Washed tissue slabs were then incubated in the eMAP hydrogel monomer solution for 1 to 2 days at 4°C while shaking before proceeding with gelation. See the "Slicing and gelation" section for the gelation steps.

Both chemical and physical tissue hybrids were sectioned to 100-μm-thick tissue sections using a Vibratome (VT1000S, Leica Biosystems, Germany) for immunohistochemistry. For both primary antibody and secondary antibody labeling steps, one master mix of antibodies in PBST was prepared to account for both chemical hybrid and physical hybrid replicates, which was then split evenly to ensure that every well contained the same amount of probes. Primary antibody labeling step was done overnight at RT. Samples were then washed for 3 to 5 hours with three solution exchanges in PBST. Secondary antibody labeling step was also done overnight at RT followed by 3 to 5 hours of washing in PBST with three solution exchanges. Labeled samples were expanded in DI water for 30 min before imaging.

For antibody compatibility in Marmoset brains, we tested the antibodies on eMAP-processed brain tissues harvested from a single animal. The success or failure of antibody labeling was decided on the basis of the staining patterns seen in the mouse brains.

In utero electroporation

All animal experiments were approved by the MIT Committee on Animal Care and meet the NIH guidelines for the use and care of vertebrate animals. In utero electroporation of E15.5-timed pregnant C57BL/6J mice was performed to label L2/3 cortical pyramidal neurons, as previously described (*45*). Animals were coelectroporated with approximately 1 μl of Cre-dependent constructs expressing eYFP (0.7 μg/μl) and a plasmid expressing Cre recombinase (0.04 μg/μl) with 0.1% Fast Green for visualization. A total of 0.75 μl of the plasmid solution was injected into the right lateral ventricle with a 32-gauge Hamilton syringe (Hamilton Company). Five pulses of 36 V (duration, 50 ms; frequency, 1 Hz) targeting the visual cortex were delivered from a square-wave electroporator (ECM830, Harvard Apparatus) using 5-mm-diameter platinum electrodes (Protech International).

Cranial window implantation

After in utero electroporation, pups were reared to adulthood (postnatal days 42 to 57) and implanted with a 5-mm cranial window over the right hemisphere as described (*46*). Sulfamethoxazole (1 mg/ml) and trimethoprim (0.2 mg/ml) were chronically administered in the drinking water to maintain optical clarity of implanted windows.

Two-photon imaging

Imaging was performed on a custom-built two-photon microscope with custom acquisition software as previously described (*24*). Briefly, mice were anesthetized with isoflurane (0.75 to 1.25%) and secured in a stereotaxic frame. YFP was excited with a Mai Tai HP Ti:Sapphire laser (Spectra-Physics) at 915 nm. After scanning with galvanometric XY-scanning mirrors (6215H, Cambridge Technology) and a piezo actuator *Z*-positioning system (Piezosystem Jena), the laser beam was focused by a 20×/1.0-NA water immersion objective lens (W Plan-Apochromat, Zeiss) to the same focal volume location in the specimen. The laser produces ~100-fs unsynchronized pulses at a rate of 80 MHz, and the final power onto the window ranges from approximately 35 to 50 mW. The emission signals were collected by the same objective lens, passed through an infrared blocking filter, and separated by dichroic mirrors and bandpass filters to collect the YFP emission signal from 520 to 560 nm onto a photomultiplier tube. Imaging was performed at high resolution (250 nm/pixel *XY* resolution, 0.9 μm/frame *Z* resolution). Two-photon raw scanner data were processed for spectral linear unmixing and converted into a red-green-blue (RGB) image *z* stack using MATLAB and ImageJ (NIH).

Multiround staining of inhibitory synapses

The eMAP-processed trimmed section containing the target cell was incubated with primary antibodies in 0.5 to 1 ml of PBST at RT for 1 to 4 days, followed by washing at RT in PBST three times over 6 to 24 hours. The section was then incubated with secondary antibodies in 300 to 500 μl of PBST at RT for 1 to 2 days, followed by washing at RT in PBST three times over 6 to 24 hours. Primary antibodies were directed against GFP (chicken, Invitrogen, A10262), $GABA_AR\alpha1$ (rabbit, Synaptic Systems, 224203), $GABA_AR\beta3$ (mouse, BioLegend, 818501), VGAT (rabbit, Millipore, AB5062P), GAD2 (mouse, BioLegend, 844502), and Gephyrin (mouse, BD, 612632). Anti-GFP was included in each of the three rounds to identify the YFP dendritic fill, which was used for alignment between rounds. Round 1 also included $GABA_AR\alpha1$/$GABA_AR\beta3$, round 2 included VGAT/GAD2, and round 3 included Gephyrin. Secondary antibodies used included anti-chicken immunoglobulin Y (IgY) (Alexa Fluor 647, Abcam, ab150175), anti-rabbit IgG (Alexa Fluor Plus 488, Invitrogen, A32731), and anti-mouse IgG (Alexa Fluor 568, Abcam, ab175473). High concentrations of both primary and secondary antibodies were used with the goal of saturating all antigen targets throughout the sample. Primary antibodies were used at the following volumes: GFP (5 to 10 μl) and $GABA_AR\alpha1$/$GABA_AR\beta3$/VGAT/GAD2/Gephyrin (10 to 40 μl). Secondary antibodies were used at the same volume of the corresponding primary antibody, with the exception of the secondary antibody for anti-GFP, which was used at two times the volume of the primary antibody.

Before mounting and imaging, the eMAP-processed immunostained section was further expanded in a dilute buffer [either 0.005 to 0.02× PBS or 0.1 mM tris (RDD008, MilliporeSigma)] and allowed to stabilize for at least 1 hour before imaging. Expanded samples were mounted on a 60-mm-diameter petri dish and covered with a glass-bottom Willco dish (HBSB-5030, WillCo Wells, Amsterdam, The Netherlands) secured with Blu-Tack adhesive. The Willco dish was supported over the petri dish with stacked glass coverslips surrounding the sample. The space between the Willco dish and petri dish, and surrounding the sample, was filled with the expansion buffer, avoiding contact with the Blu-Tack. eMAP samples were imaged on the Leica TCS SP8 microscope system with a 63×, 1.30-NA glycerol immersion objective with a white-light tunable laser source. Images were acquired with 75 nm/pixel *XY* and 0.66 μm/frame *Z* resolution. Wide-field whole-cell images of the anti-GFP–labeled channel were also obtained by a *z*-stack acquisition with a 10×, 0.3-NA water immersion objective.

eMAP from rounds 1, 2, and 3 of antibody staining were aligned using the Fijiyama plugin for Fiji/ImageJ (https://imagej.net/Fijiyama). First, the GFP channel of round 2 was aligned onto the GFP channel

of round 3, and then the round 1 GFP channel was aligned onto the round 3 GFP channel, with a further optimization by aligning the $GABA_AR\alpha1$ channel to the Gephyrin channel. Then, the R1/3 hyperstack was aligned onto the R2/3 hyperstack to create an eight-channel hyperstack, which was used for bouton content analysis. Seven dendritic segments were successfully aligned between all three rounds, with an average length of 18.3 μm (unexpanded). Because the fidelity of alignment decreases with increasing distance from the GFP-filled dendrite, only boutons within 60 μm of the dendrite were scored (10.7 μm unexpanded).

Boutons were scored manually by placing markers using a modified version of the ObjectJ plugin for Fiji/ImageJ (*24*). Markers were placed denoting the presence of various postsynaptic ($GABA_AR\alpha1$, $GABA_AR\beta3$, and Gephyrin) markers in boutons that contained both VGAT and GAD2 and met a volume threshold of at least 100 voxels, which represents approximately 1.38 μm^3 expanded or 0.00766 μm^3 unexpanded. Postsynaptic puncta were scored if they met a size threshold of at least seven voxels, which represents approximately 0.097 μm^3 in the expanded volume or 0.0005 μm^3 (0.097/5.6^3 μm^3) unexpanded. A total of 497 boutons were counted. For figures, some images were processed using the ImageJ smooth command. The display range for each channel was manually adjusted linearly.

Axial and radial analyses

Images were normalized by 99.99 percentile intensity and denoised with a total-variation noise reduction algorithm (*47*). To automatically locate synapses, Gaussian blur followed by the blob detection using the determinant of Hessian was carried out on a postsynaptic scaffolding (PSD-95) channel. On the basis of the centroids of the detected blobs, image blocks were extracted with a size of z (D) × 70 (H) × 70 (W). The image blocks containing a synapse were used for the axial and radial analyses.

To measure the distance between pre- and post-SyPs along the synaptic axis, the synapse image blocks were rotated about the z axis (x-y plane) to make the synaptic cleft lie in parallel on the x axis. The rotation was performed by segmenting the maximum z–projected PSD-95 channel followed by taking a rotation for the degrees between the x axis and the major axis of the ellipse overlaid on the segmented region of the PSD-95 image. The segmentation was performed by obtaining a threshold using Otsu's method and getting the morphological closing of the regions that were above the threshold. Side-view synapses that expose the lamellar structure on the x-y plane were selected for measuring the axial distance. We filtered out non–side-view synapses by examining the eccentricity of the ellipse on the PSD-95 segmentation. Image blocks that contained more than one PSD-95 segmented region were discarded. The remaining image blocks were manually examined to further discard obscure side-view synapses. To get the distance, we maximum z–projected the rotated side-view synapses and took the average for each channel in range where PSD-95 spans along the x axis. The averaged intensities were Gaussian-fitted, and the peak positions were located. The actual distance was calculated by multiplying the voxel size to the peak-to-peak distance and then adjusting the resulting value by the linear expansion factor.

To examine the radial configuration of an individual synapse, en face view synapses were manually selected. The maximum z–projected images were rotated about the z axis, as described previously. Segmentation was also performed in the same way but with an additional division process by the watershed algorithm. The r value that indicates the position with respect to the PSD-95 ellipse was calculated such that $r = (x - x_0)^2/R_x^2 + (y - y_0)^2/R_y^2$, where x and y are the centroid coordinates of the segmented region, x_0 and y_0 are the ellipse centers, and R_x and R_y are the major and minor axis lengths. The Ripley's H statistic is estimated without the edge correction, as described by Khater *et al.* (*32*). Briefly, centroid coordinates of the segmented blobs were obtained and used to calculate Ripley's H function. In this calculation, the cropped space on the x-y plane of the image block (70 pixels by 70 pixels) was used as the study area.

To compare the relative spans parallel to the synaptic cleft, the normalized and denoised images were segmented as a chunk to represent the spans within a synapse. The major axis length of the overlaying ellipse was measured for the resulting segmented chunks, and this was separately performed for each channel. In this analysis, we assumed that the major axes are nearly parallel to the synaptic cleft, and the ratio of the spans is irrelevant to the viewing angles of synapses.

Microtubule peak-to-peak distance measurement

Formaldehyde-fixed mouse brain tissues were sliced to 100-μm-thick sections and then eMAP-processed for four rounds to achieve ~10× expansion, as described previously. The 4×-embedded samples were labeled with β-tubulin antibody (ab6046, Abcam) at 1:300 dilution in PBST at RT overnight. Samples were washed for 3 to 5 hours with three solution exchanges and then labeled with secondary antibodies (111-547-008, Jackson ImmunoResearch) at RT overnight. Stained samples were expanded in DI water for 30 min at RT before imaging. The samples were imaged with 63× 1.2-NA water immersion objective described previously. Pinhole size was reduced to 0.5 Airy Unit (AU) for improved resolution in exchange for some loss in signal intensity.

Rectangular regions containing a clearly isolatable microtubule were manually segmented from the raw images using Fiji. Transverse line intensity profiles across the microtubules were obtained using the Plot Profile function on Fiji.

The acquired intensity profiles were fitted with the sum of two Gaussians. The distance between the two estimated means was considered as the peak-to-peak distance. The peak-to-peak distances from multiple measures ($n = 50$) were collected and averaged to give the mean and the SD of the distance.

Meso- and microscale distortion analysis

For mesoscale distortion analysis, 4% formaldehyde–fixed mouse brain tissues were sliced to 200-μm-thick sections and then stained with DyLight 488–conjugated Tomato Lectin (DL-1171-1, Vector Laboratories, 1:100 dilution) and 4′,6-diamidino-2-phenylindole (DAPI; D1306, Invitrogen) in PBST at RT overnight. After 3 to 5 hours of washing with three solution exchanges, each sample was imaged with careful documentation of the sample orientation and the location of the imaged region. The imaged tissue samples were then incubated in eMAP hydrogel monomer solution for 1 day at 4°C while shaking and then gelled, as previously described. Because DyLight 488–conjugated Tomato Lectin signal does not survive the eMAP processing, the eMAP-processed samples were labeled with DyLight 649–conjugated Tomato Lectin (DL-1178-1, Vector Laboratories, 1:100 dilution) and DAPI. After expanding the labeled tissue in DI water, previously imaged regions for each sample were identified under the microscope using previous documentation and DAPI labeling as a guide and then imaged for the distortion analysis.

For microscale distortion analysis, 4% formaldehyde–fixed mouse brain tissues were sliced to 200-μm-thick sections and then stained

with anti–NF-H antibody (PA1-10002, Invitrogen), Alexa Fluor 488–conjugated anti-chicken secondary antibody (ab150169, Abcam), and DAPI. Primary and secondary antibodies were labeled separately. Each sample was imaged with careful documentation of the sample orientation and the location of the imaged region. The imaged samples were eMAP-processed and then labeled again with anti–NF-H antibody (PA1-10002, Invitrogen) and DAPI. Secondary antibody was switched to Alexa Fluor 647–conjugated anti-chicken antibody (ab150175, Abcam) for post-expansion imaging. After expanding the labeled tissue in DI water, previously imaged regions for each sample were identified under the microscope using previous documentation and DAPI labeling as a guide and then imaged for distortion analysis.

The distortion error was defined and calculated as previously described (*10*) with some minor modifications. Briefly, we took the images of corresponding regions in pre- and post-eMAP tissues and carried out a series of preprocessing, including manual prealignment, rescaling, noise reduction, Gaussian blur (to match the blurriness in pre-expansion), and binarization, before performing image registration to measure the distortion. Using Elastix (*48*), the image registration for pre- and post-expansion images was carried out in two steps. First, to eliminate the errors caused by the sample mounting, pre- and post-expansion images were registered by affine transformation. Then, the rigidly aligned post-expansion image was registered by the b-spline nonrigid registration to measure the distortion accompanied by tissue expansion. A portion of points on the foreground of the binarized post-expansion image were randomly selected, and the Euclidean distances between every possible pair of points were calculated. The difference in the distance between the corresponding pairs of points in pre- and post-expansion images was considered as the distortion error. The RMSE at each measurement length from multiple samples was sorted out and summarized by the average and SD of RMSE across the measurement lengths.

SUPPLEMENTARY MATERIALS

Supplementary material for this article is available at https://science.org/doi/10.1126/sciadv.abf6589

View/request a protocol for this paper from *Bio-protocol*.

REFERENCES AND NOTES

1. K. Chung, J. Wallace, S.-Y. Kim, S. Kalyanasundaram, A. S. Andalman, T. J. Davidson, J. J. Mirzabekov, K. A. Zalocusky, J. Mattis, A. K. Denisin, S. Pak, H. Bernstein, C. Ramakrishnan, L. Grosenick, V. Gradinaru, K. Deisseroth, Structural and molecular interrogation of intact biological systems. *Nature* **497**, 332–337 (2013).
2. F. Chen, P. W. Tillberg, E. S. Boyden, Expansion microscopy. *Science* **347**, 543–548 (2015).
3. H. R. Ueda, A. Ertürk, K. Chung, V. Gradinaru, A. Chédotal, P. Tomancak, P. J. Keller, Tissue clearing and its applications in neuroscience. *Nat. Rev. Neurosci.* **21**, 61–79 (2020).
4. A. T. Wassie, Y. Zhao, E. S. Boyden, Expansion microscopy: Principles and uses in biological research. *Nat. Methods* **16**, 33–41 (2019).
5. S. W. Choi, W. Guan, K. Chung, Basic principles of hydrogel-based tissue transformation technologies and their applications. *Cell* **184**, 4115–4136 (2021).
6. T. Ku, J. Swaney, J.-Y. Park, A. Albanese, E. Murray, J. H. Cho, Y.-G. Park, V. Mangena, J. Chen, K. Chung, Multiplexed and scalable super-resolution imaging of three-dimensional protein localization in size-adjustable tissues. *Nat. Biotechnol.* **34**, 973–981 (2016).
7. H.-E. Park, D. Choi, J. S. Park, C. Sim, S. Park, S. Kang, H. Yim, M. Lee, J. Kim, J. Pac, K. Rhee, J. Lee, Y. Lee, Y. Lee, S.-Y. Kim, Scalable and isotropic expansion of tissues with simply tunable expansion ratio. *Adv. Sci.* **6**, 1901673 (2019).
8. J.-B. Chang, F. Chen, Y.-G. Yoon, E. E. Jung, H. Babcock, J. S. Kang, S. Asano, H.-J. Suk, N. Pak, P. W. Tillberg, A. T. Wassie, D. Cai, E. S. Boyden, Iterative expansion microscopy. *Nat. Methods* **14**, 593–599 (2017).
9. P. W. Tillberg, F. Chen, K. D. Piatkevich, Y. Zhao, C.-C. J. Yu, B. P. English, L. Gao, A. Martorell, H.-J. Suk, F. Yoshida, E. M. DeGennaro, D. H. Roossien, G. Gong, U. Seneviratne, S. R. Tannenbaum, R. Desimone, D. Cai, E. S. Boyden, Protein-retention expansion microscopy of cells and tissues labeled using standard fluorescent proteins and antibodies. *Nat. Biotechnol.* **34**, 987–992 (2016).
10. T. J. Chozinski, A. R. Halpern, H. Okawa, H.-J. Kim, G. J. Tremel, R. O. L. Wong, J. C. Vaughan, Expansion microscopy with conventional antibodies and fluorescent proteins. *Nat. Methods* **13**, 485–488 (2016).
11. D. Gambarotto, V. Hamel, P. Guichard, Ultrastructure expansion microscopy (U-ExM). *Methods Cell Biol.* **161**, 57–81 (2021).
12. T. Ku, W. Guan, N. B. Evans, C. H. Sohn, A. Albanese, J.-G. Kim, M. P. Frosch, K. Chung, Elasticizing tissues for reversible shape transformation and accelerated molecular labeling. *Nat. Methods* **17**, 609–613 (2020).
13. H. Nishimune, Y. Badawi, S. Mori, K. Shigemoto, Dual-color STED microscopy reveals a sandwich structure of Bassoon and Piccolo in active zones of adult and aged mice. *Sci. Rep.* **6**, 27935 (2016).
14. M. Y. Ahmed, B. A. Chioza, A. Rajab, K. Schmitz-Abe, A. Al-Khayat, S. Al-Turki, E. L. Baple, M. A. Patton, A. Y. Al-Memar, M. E. Hurles, J. N. Partlow, R. S. Hill, G. D. Evrony, S. Servattalab, K. Markianos, C. A. Walsh, A. H. Crosby, G. H. Mochida, Loss of PCLO function underlies pontocerebellar hypoplasia type III. *Neurology* **84**, 1745–1750 (2015).
15. D. Sato, A. C. Lionel, C. S. Leblond, A. Prasad, D. Pinto, S. Walker, I. O'Connor, C. Russell, I. E. Drmic, F. F. Hamdan, J. L. Michaud, V. Endris, R. Roeth, R. Delorme, G. Huguet, M. Leboyer, M. Rastam, C. Gillberg, M. Lathrop, D. J. Stavropoulos, E. Anagnostou, R. Weksberg, E. Fombonne, L. Zwaigenbaum, B. A. Fernandez, W. Roberts, G. A. Rappold, C. R. Marshall, T. Bourgeron, P. Szatmari, S. W. Scherer, SHANK1 deletions in males with autism spectrum disorder. *Am. J. Hum. Genet.* **90**, 879–887 (2012).
16. V. Salpietro, C. L. Dixon, H. Guo, O. D. Bello, J. Vandrovcova, S. Efthymiou, R. Maroofian, G. Heimer, L. Burglen, S. Valence, E. Torti, M. Hacke, J. Rankin, H. Tariq, E. Colin, V. Procaccio, P. Striano, K. Mankad, A. Lieb, S. Chen, L. Pisani, C. Bettencourt, R. Männikkö, A. Manole, A. Brusco, E. Grosso, G. B. Ferrero, J. Armstrong-Moron, S. Gueden, O. Bar-Yosef, M. Tzadok, K. G. Monaghan, T. Santiago-Sim, R. E. Person, M. T. Cho, R. Willaert, Y. Yoo, J.-H. Chae, Y. Quan, H. Wu, T. Wang, R. A. Bernier, K. Xia, A. Blesson, M. Jain, M. M. Motazacker, B. Jaeger, A. L. Schneider, K. Boysen, A. M. Muir, C. T. Myers, R. H. Gavrilova, L. Gunderson, L. Schultz-Rogers, E. W. Klee, D. Dyment, M. Osmond, M. Parellada, C. Llorente, J. Gonzalez-Peñas, A. Carracedo, A. Van Haeringen, C. Ruivenkamp, C. Nava, D. Heron, R. Nardello, M. Iacomino, C. Minetti, A. Skabar, A. Fabretto; SYNAPS Study Group, M. Raspall-Chaure, M. Chez, A. Tsai, E. Fassi, M. Shinawi, J. N. Constantino, R. De Zorzi, S. Fortuna, F. Kok, B. Keren, D. Bonneau, M. Choi, B. Benzeev, F. Zara, H. C. Mefford, I. E. Scheffer, J. Clayton-Smith, A. Macaya, J. E. Rothman, E. E. Eichler, D. M. Kullmann, H. Houlden, AMPA receptor GluA2 subunit defects are a cause of neurodevelopmental disorders. *Nat. Commun.* **10**, 3094 (2019).
17. G. Nyíri, T. F. Freund, P. Somogyi, Input-dependent synaptic targeting of α2-subunit-containing GABAA receptors in synapses of hippocampal pyramidal cells of the rat. *Eur. J. Neurosci.* **13**, 428–442 (2001).
18. A. Hsu, J. I. Luebke, M. Medalla, Comparative ultrastructural features of excitatory synapses in the visual and frontal cortices of the adult mouse and monkey. *J. Comp. Neurol.* **525**, 2175–2191 (2017).
19. T. Klausberger, J. D. B. Roberts, P. Somogyi, Cell type- and input-specific differences in the number and subtypes of synaptic GABA(A) receptors in the hippocampus. *J. Neurosci.* **22**, 2513–2521 (2002).
20. C. Q. Chiu, J. S. Martenson, M. Yamazaki, R. Natsume, K. Sakimura, S. Tomita, S. J. Tavalin, M. J. Higley, Input-specific NMDAR-dependent potentiation of dendritic GABAergic inhibition. *Neuron* **97**, 368–377.e3 (2018).
21. M. Fagiolini, J.-M. Fritschy, K. Löw, H. Möhler, U. Rudolph, T. K. Hensch, Specific GABAA circuits for visual cortical plasticity. *Science* **303**, 1681–1683 (2004).
22. B. Lüscher, C. A. Keller, Regulation of GABAA receptor trafficking, channel activity, and functional plasticity of inhibitory synapses. *Pharmacol. Ther.* **102**, 195–221 (2004).
23. J. L. Chen, K. L. Villa, J. W. Cha, P. T. C. So, Y. Kubota, E. Nedivi, Clustered dynamics of inhibitory synapses and dendritic spines in the adult neocortex. *Neuron* **74**, 361–373 (2012).
24. K. L. Villa, K. P. Berry, J. Subramanian, J. W. Cha, W. Chan Oh, H.-B. Kwon, Y. Kubota, P. T. C. So, E. Nedivi, Inhibitory synapses are repeatedly assembled and removed at persistent sites in vivo. *Neuron* **90**, 662–664 (2016).
25. J. Subramanian, K. Michel, M. Benoit, E. Nedivi, CPG15/Neuritin mimics experience in selecting excitatory synapses for stabilization by facilitating PSD95 recruitment. *Cell Rep.* **28**, 1584–1595.e5 (2019).
26. A. Dani, B. Huang, J. Bergan, C. Dulac, X. Zhuang, Superresolution imaging of chemical synapses in the brain. *Neuron* **68**, 843–856 (2010).
27. M. Masugi-Tokita, E. Tarusawa, M. Watanabe, E. Molnár, K. Fujimoto, R. Shigemoto, Number and density of AMPA receptors in individual synapses in the rat cerebellum as revealed by SDS-digested freeze-fracture replica labeling. *J. Neurosci.* **27**, 2135–2144 (2007).

28. T. P. Li, Y. Song, H. D. MacGillavry, T. A. Blanpied, S. Raghavachari, Protein crowding within the postsynaptic density can impede the escape of membrane proteins. *J. Neurosci.* **36**, 4276–4295 (2016).
29. M. Schoen, J. M. Reichel, M. Demestre, S. Putz, D. Deshpande, C. Proepper, S. Liebau, M. J. Schmeisser, A. C. Ludolph, J. Michaelis, T. M. Boeckers, Super-resolution microscopy reveals presynaptic localization of the ALS/FTD related protein FUS in hippocampal neurons. *Front. Cell. Neurosci.* **9**, 496 (2016).
30. E. D. Gundelfinger, C. Reissner, C. C. Garner, Role of bassoon and piccolo in assembly and molecular organization of the active zone. *Front. Synaptic Neurosci.* **7**, 19 (2015).
31. J. Zhang, J. S. Diamond, Distinct perisynaptic and synaptic localization of NMDA and AMPA receptors on ganglion cells in rat retina. *J. Comp. Neurol.* **498**, 810–820 (2006).
32. I. M. Khater, I. R. Nabi, G. Hamarneh, A review of super-resolution single-molecule localization microscopy cluster analysis and quantification methods. *Patterns Prejud.* **1**, 100038 (2020).
33. C. T. Miller, W. A. Freiwald, D. A. Leopold, J. F. Mitchell, A. C. Silva, X. Wang, Marmosets: A neuroscientific model of human social behavior. *Neuron* **90**, 219–233 (2016).
34. E. Sasaki, H. Suemizu, A. Shimada, K. Hanazawa, R. Oiwa, M. Kamioka, I. Tomioka, Y. Sotomaru, R. Hirakawa, T. Eto, S. Shiozawa, T. Maeda, M. Ito, R. Ito, C. Kito, C. Yagihashi, K. Kawai, H. Miyoshi, Y. Tanioka, N. Tamaoki, S. Habu, H. Okano, T. Nomura, Generation of transgenic non-human primates with germline transmission. *Nature* **459**, 523–527 (2009).
35. N. Kishi, K. Sato, E. Sasaki, H. Okano, Common marmoset as a new model animal for neuroscience research and genome editing technology. *Develop. Growth Differ.* **56**, 53–62 (2014).
36. C. G. Jennings, R. Landman, Y. Zhou, J. Sharma, J. Hyman, J. Anthony Movshon, Z. Qiu, A. C. Roberts, A. W. Roe, X. Wang, H. Zhou, L. Wang, F. Zhang, R. Desimone, G. Feng, Opportunities and challenges in modeling human brain disorders in transgenic primates. *Nat. Neurosci.* **19**, 1123–1130 (2016).
37. J. E. Park, A. C. Silva, Generation of genetically engineered non-human primate models of brain function and neurological disorders. *Am. J. Primatol.* **81**, e22931 (2019).
38. J. E. Park, X. F. Zhang, S.-H. Choi, J. Okahara, E. Sasaki, A. C. Silva, Generation of transgenic marmosets expressing genetically encoded calcium indicators. *Sci. Rep.* **6**, 34931 (2016).
39. K. Servick, "Why are U.S. neuroscientists clamoring for marmosets?" *Science*, 23 October 2018; doi:10.1126/science.aav8223.
40. T. Aida, G. Feng, The dawn of non-human primate models for neurodevelopmental disorders. *Curr. Opin. Genet. Dev.* **65**, 160–168 (2020).
41. G. Lima Caldeira, J. Peça, A. L. Carvalho, New insights on synaptic dysfunction in neuropsychiatric disorders. *Curr. Opin. Neurobiol.* **57**, 62–70 (2019).
42. T. Bourgeron, From the genetic architecture to synaptic plasticity in autism spectrum disorder. *Nat. Rev. Neurosci.* **16**, 551–563 (2015).
43. M. Cizeron, Z. Qiu, B. Koniaris, R. Gokhale, N. H. Komiyama, E. Fransén, S. G. N. Grant, A brain-wide atlas of synapses across the mouse lifespan. *Science* **369**, 270–275 (2020).
44. F. Zhu, M. Cizeron, Z. Qiu, R. Benavides-Piccione, M. V. Kopanitsa, N. G. Skene, B. Koniaris, J. DeFelipe, E. Fransén, N. H. Komiyama, S. G. N. Grant, Architecture of the mouse brain synaptome. *Neuron* **99**, 781–799.e10 (2018).
45. H. Tabata, K. Nakajima, Efficient in utero gene transfer system to the developing mouse brain using electroporation: Visualization of neuronal migration in the developing cortex. *Neuroscience* **103**, 865–872 (2001).
46. W.-C. A. Lee, J. L. Chen, H. Huang, J. H. Leslie, Y. Amitai, P. T. So, E. Nedivi, A dynamic zone defines interneuron remodeling in the adult neocortex. *Proc. Natl. Acad. Sci. U.S.A.* **105**, 19968–19973 (2008).
47. A. Chambolle, An algorithm for total variation minimization and applications. *J. Math. Imag. Vis.* **20**, 89–97 (2004).
48. S. Klein, M. Staring, K. Murphy, M. A. Viergever, J. P. W. Pluim, elastix: A toolbox for intensity-based medical image registration. *IEEE Trans. Med. Imaging* **29**, 196–205 (2010).

Acknowledgments: We thank the entire Chung laboratory for support and discussions. We thank K. Xie and Y. Tian for mouse sample preparation and A. Albanese and W. Guan for helping optimize the protocol. We thank Y. Hou for marmoset sample preparation. **Funding:** K.C. was supported by the Burroughs Wellcome Fund Career Awards at the Scientific Interface, the Searle Scholars Program, the Packard Award in Science and Engineering, the NARSAD Young Investigator Award, the Institute for Basic Science (grant no. IBS-R026-D1), and the McKnight Foundation Technology Award. This work was supported by the JPB Foundation, the NCSOFT Cultural Foundation, and the NIH (grant R01-EY025437 to E.N. and DP2-ES027992 to K.C.). **Author contributions:** Joha Park, S.K., D.H.Y., and K.C. designed the experiments. T.K. developed the physical hybridization protocol and collected initial results. S.K. and D.H.Y., with help from Juhyuk Park, performed the eMAP tissue processing and imaging. Joha Park performed image processing and the computational analyses. K.L.V. and J.E.L., with help from T.K., performed the experiments and analyzed images related to the inhibitory synapse $GABA_A$ receptor composition. G.F. and Q.Z. provided marmoset brain tissues and helped design the marmoset brain–related experiments. Joha Park, S.K., D.H.Y., K.L.V., J.E.L., and K.C. wrote the manuscript with input from all other authors. E.N. supervised the inhibitory synapse experiments and data analysis. K.C. supervised all aspects of the work. **Competing interests:** K.C. and T.K. are coinventors on a patent application owned by MIT covering the MAP technology (U.S. Provisional Patent Application 62/330,018). K.C. is a cofounder of LifeCanvas Technologies, a startup that provides solutions for 3D tissue processing and analysis. **Data and materials availability:** All data needed to evaluate the conclusions in the paper are present in the paper and/or the Supplementary Materials. Microscopy imaging datasets and custom codes have been archived in Zenodo (10.5281/zenodo.5229051). Resources that may help enable general users to establish the methodology are freely available online (http://chunglabresources.org).

Submitted 10 November 2020
Accepted 24 September 2021
Published 12 November 2021
10.1126/sciadv.abf6589

Epitope-preserving magnified analysis of proteome (eMAP)

Joha ParkSarim KhanDae Hee YunTaeyun KuKatherine L. VillaJiachen E. LeeQiangge ZhangJuhyuk ParkGuoping FengElly NediviKwanghun Chung

Sci. Adv., 7 (46), eabf6589. • DOI: 10.1126/sciadv.abf6589